Optimal Design of Thermoelectric Generators Embedded in a Thermal Resistance Network

Submitted by
Elizabeth Brownell

IN PARTIALL FULFILLMENT OF THE REQUIREMENTS FOR THE DEGREE OF
MASTER OF SCIENCE IN MECHANICAL ENGINEERING

School of Engineering
Tufts University
Medford, Massachuestts

February 2013

Author:
Elizabeth Brownell
Department of Mechanical Engineering
Tufts Univeristy

Certified by:
Associate Professor Marc Hodes
Department of Mechanical Engineering
Tufts University

Committee:
Associate Professor Luisa Chiesa
Department of Mechanical Engineering
Tufts University

Committee:
Martin Cleary
Postdoctoral Scientist
Massachusetts Institute of Technology

ABSTRACT

Optimal Design of Thermoelectric Generators Embedded in a Thermal Resistance Network

by

Elizabeth Brownell

Chair: Marc Hodes

A procedure to optimize the height and number of semiconductor pellets in a thermoelectric generator (TEG) embedded in a thermal resistance network to maximize its performance (output power) or efficiency is provided. Prescribed are the required thermophysical properties of the pellets, temperature difference across the system, total footprint of thermoelectric material, relevant thermal resistances, electrical contact resistance at the interconnects between the pellets, and load resistance in a TEG. When efficiency is maximized, performance is also prescribed and it is implied that its value is below its maximum. The temperature difference imposed across the pellets in the TEG is assumed to be small enough that their thermophysical properties may be approximated as constants and the use of a single thermoelectric material is appropriate. Examples illustrate the use of the optimization procedure. The sensitivity of maximal performance to variations in the relevant thermal resistances, electrical contact resistance, and load resistance is quantified.

ACKNOWLEDGMENT

I would like to extend my sincerest thanks to my advisor, Dr. Marc Hodes, who has provided an incredibly supportive environment to create this research in. His guidance and knowledge have made this work possible, and his patience and encouragement have allowed me to thrive as a student. I could not ask for a better advisor, and I am forever grateful to him.

Many thanks also go to my committee members, Professor Luisa Chiesa and Martin Cleary, for their advice, feedback, and support. I gratefully acknowledge the Wittich Energy Sustainability Research Initiation Fund for supporting this research. Finally, I would like to thank my colleagues, friends and family for their undying support and encouragement throughout my career as a graduate student.

CONTENTS

LIST OF TABLES

LIST OF FIGURES

NOMENCLATURE

A_e	Total footprint of thermoelectric material [m^2].
A_p	Cross-sectional area of pellet [m^2].
A_{sub}	Total footprint of TEM [m^2]
csi	Cold-side interface.
k	Thermal conductivity [$W/(m \cdot K)$].
K_{i-j}	Thermal conductance between nodes 'i' and 'j' [W/K].
K''_{i-j}	Flux-based thermal conductance between nodes 'i' and 'j,' K_{i-j}/A_{sub} [$W/\left(m^2 \cdot K\right)$]
H	Pellet height [mm].
hsi	Hot-side interface.
I	Current [A].
N	Number of thermocouples.
q	Rate of heat transfer [W].
R	Bulk Ohmic resistance of thermocouple [Ω].
R_{ec-R}	Electrical contact resistance of thermocouple [Ω].
$R_{ec-\rho}$	Electrical contact resistivity [$\Omega \cdot m^2$].
T	Temperature [K].
TEG	Thermoelectric generator
TEM	Thermoelectric module
V_{TEM}	Voltage difference across TEM, $V_o - V_N$ [V].
$\dot{W}_g$	Output power of TEM [W].
Z	Figure of merit of thermocouple [$1/K$].

Greek Symbols

α_i	Seebeck coefficient of pellet type 'i' $[V/K]$.
$\alpha_{p,n}$	$\alpha_p - \alpha_n$ $[V/K]$.
ρ	Electrical resistivity $[\Omega \cdot m]$.

SUBSCRIPTS

c	cold-side interface (csi).
h	hot-side interface (hsi).
n	n-type pellet.
opt	conditions at optimal performance or efficiency.
p	p-type pellet.
∞, c	cold-side ambient.
∞, h	hot-side ambient.

I INTRODUCTION

1.1 Thermoelectric Modules and Generators

Thermoelectric modules (TEMs) are solid-state devices which can act as coolers, heaters or generators by exploiting the thermoelectric effects [15]. In precision temperature control applications, applying the necessary voltage difference across a TEM causes it to absorb or evolve heat at the required rate on the side of it to which a component is attached [31]. Acting as a thermoelectric generator, or TEG, it generates power when a temperature difference is maintained across it [3].

TEGs are well adapted for power production in remote or inaccessible locales, such as in powering spacecraft [11], where a reliable and durable solid-state generator is required. They have also been used for small scale generation to power implanted pacemakers. The heat source for the TEGs in these applications is provided by a radioisotope [17]. Power for wristwatches and small personal electronics can be supplemented by TEGs running on body heat [14, 23].

Waste heat recovery is a major target market for TEGs. Industrial process efficiencies can be improved and vehicular electrical systems supplemented by reusing waste heat from manufacturing processes and exhaust fumes, respectively [4, 5, 12, 13, 23, 27]. Increasing TEG output power and efficiency makes them a more viable option in such applications and for providing clean power generation in small-scale applications. We provide a procedure to optimize the geometry (height and number) of the pellets in a TEG to accomplish this, subject to the constraints discussed in §2.1.

1.2 TEM Design

A schematic of a TEM is shown in Fig. 1. Its principal elements are the semiconductor pellets. The alternating n- and p-type pellets are connected in series by electrical interconnects (typically

copper) to either a power source (for coolers/heaters) or a load (for generators). Each adjacent pair of n- and p-type pellets is referred to as a thermocouple, and a TEM has N thermocouples. The interconnected thermocouples are enclosed by ceramic substrates, which connect them thermally in parallel.

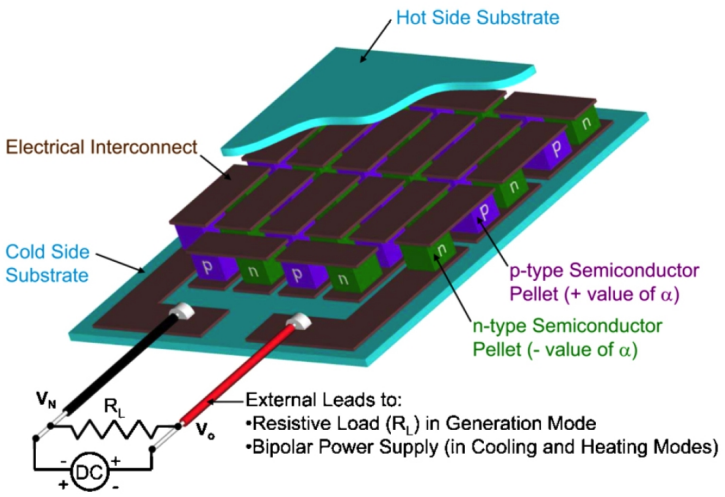

Figure 1: Schematic of a TEM.

During TEG operation, the cold side is that connected to the external leads, as per Fig. 2 (bottom), a schematic of a two-thermocouple TEG. The voltage in the external lead connected to the n-type pellet on the cold side of the TEM is denoted by V_o and that in the other lead by V_N. The hot-side interface (hsi) is defined as that between the thermocouples and the electrical interconnects on the side of the TEM which is coupled to the heat source, as per Fig. 2 (left). The cold-side interface (csi) is defined analogously on the side coupled to the heat sink. The temperatures at the hsi and csi are denoted by T_h and T_c, respectively.

The semiconducting materials which comprise the pellets, such as bismuth telluride or lead telluride, are chosen to have superior thermoelectric properties in their operating temperature range. For small operating temperature differences ($T_h - T_c \lesssim 100^\circ$ C), the pellets will usually be one homogeneous semiconducting material. For larger temperature differences, the pellets may be segmented into multiple layers, each made of a material which is operating in a more narrow temperature range where it has higher performance [12, 19].

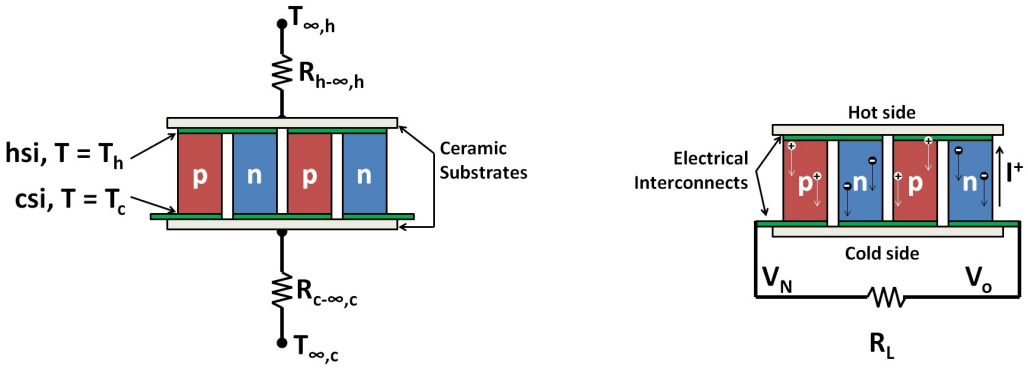

Figure 2: Thermal (left) and electrical (right) schematics of two-thermocouple TEM operating in generation mode.

As a result of the spacing between adjacent pellets, the footprint of a TEM (A_{sub}) is larger than the area occupied by thermoelectric material. The effective area of a TEM (A_e) is defined as the total footprint of the pellets, i.e., $A_e = 2NA_p$, where A_p is the cross-sectional area of a pellet. The pellet packing density (ϕ) is the fraction of a TEM's footprint that is occupied by pellets such that $\phi = A_e/A_{sub}$.

1.3 Irreversible and Thermoelectric Effects

Irreversible Ohmic heating and heat conduction and the reversible thermoelectric effects are the physical phenomena that govern TEM operation. Ohmic heating generates heat irreversibly when current flows through a conductor or semiconductor. It occurs both in the bulk of a thermocouple as well as at the interconnects due to their electrical contact resistance. Heat conduction through a TEM obeys Fourier's law, and can be approximated as being one-dimensional. When a TEM is embedded in a thermal resistance network, additional irreversibilities are associated with the heat transfer between it and the local ambient.

The thermoelectric effects, in contrast, are reversible phenomena resulting in direct conversion between thermal and electrical energy. The Seebeck effect is a bulk effect that generates an electric potential gradient in a conductor subjected to a temperature gradient under open circuit conditions. It arises because thermal diffusion causes a flow of charge carriers (electrons or holes) along (or against) temperature gradients in conducting materials, thereby generating an

electric potential gradient. In an open circuit at equilibrium, the flow of charge carriers due to electrostatic forces balances that due to thermal diffusion. The Seebeck effect is described by $V = \int_{T_c}^{T_h} \alpha(T) dT$, where $\alpha(T)$ is the temperature-dependent Seebeck coefficient [15, 24]. Conductors exhibit both positive and negative values of the Seebeck coefficient as a consequence of how well they scatter high and low energy electrons. The Seebeck coefficient can be a substantial function of temperature. It is low in metals, but moderate in certain semiconductors [15].

The Peltier effect causes energy to be evolved or absorbed when current flows through the interface between two conductors. This is because the moving charge carriers comprising an electric current (I) carry different amounts of electrical energy in different conductors. The rate of reversible heat absorption (q) at the interface equals $q = IT\left(\alpha_P - \alpha_N\right)$, where current is positive when positive charge carriers flow from n- to p-type material, and T is the absolute temperature at the junction [3, 15].

When current flows through a conducting material in the presence of a temperature gradient, heat is also liberated or absorbed due to the Thomson (bulk) effect. This is usually a secondary effect. The only material property required to account for all three thermoelectric effects is the Seebeck coefficient [3, 15].

1.4 Advantages, Limitations, and Enhancement of TEGs

TEGs are simple, low-weight devices which contain no moving parts, making them reliable, silent, vibrationless, and long-lasting. They can be as small as millimeters in footprint or joined into arbitrarily large arrays. They can be operated in any orientation and the amount of power generated can be tuned by varying the pellet geometry. They are also environmentally friendly when nontoxic thermoelectric and interconnect materials are selected [17]. The main disadvantages of TEGs are their low efficiencies compared to more standard technologies (such as vapor power plants), and their limited power output [17].

Clearly, it is preferable to operate TEGs at the maximum possible output power or efficiency for a given application. For waste heat applications, only the output power is relevant since the

heat is not being produced for the purpose of generating power. However, in applications with a prescribed power output, such as radioisotope-fueled TEGs that power instrumentation in spacecraft or natural gas-fueled pipeline monitoring equipment, high efficiency is desired.

Much of modern thermoelectric research focuses on improving the thermoelectric materials themselves [11, 20, 22, 26, 30]. To the extent possible, the pellets should have low electrical resistivity (ρ) to reduce Ohmic heating, low thermal conductivity (k) allowing a large temperature difference to be maintained across them, and the difference between the Seebeck coefficients of the n- and p-type materials in the thermocouple ($\alpha_{p,n} = \alpha_p - \alpha_n$) should be large to make energy conversion more efficient. The combined effect of these properties is often measured by the Figure of Merit (Z) of a thermoelectric material at a particular temperature, where ZT is defined as $\alpha_{p,n}^2/(KR)$, or $\left(\alpha_{p,n}^2 T\right)/(4k\rho)$ for a single thermocouple. The relationship between ZT and T is typically nonlinear, with each material having a maximum performance at a particular temperature, as shown in Fig. 3. While ZT is a useful metric to assess a material's performance, the individual values of k, ρ and α themselves are more illuminating. The irreversibilities of the external thermal resistances and the electrical contact resistivity at the interconnects in a TEM ($R_{ec-\rho}$) are also important in system design.

When a TEG is operating with a large temperature difference, it may be desirable to divide each pellet into multiple segments of different thermoelectric materials. By doing this, each material is operating in a more narrow temperature range where it has higher performance [12, 19]. For example, if a TEG were to operate from $0 - 700^\circ$C, Fig. 3 suggests using layers of Bi_2Te_3 adjacent to the cold side, PbTe in the middle, and $CoSb_3$ adjacent to the hot side. El Genk and Saber [12] developed a model to maximize the efficiency of a single thermocouple by optimizing the ratios of the segment lengths, the n- to p-type pellet footprints, and the resistances of the load and interconnects for a prescribed total pellet height, p-type pellet footprint, and operating conditions. Due to the larger temperature differences in the model, they accounted for the temperature dependance of the material properties using volume integral averaging, and for the Thompson effect. A TEG using segmented pellets could be further optimized by combining

the segmentation algorithm with the given procedure in which N and H are calculated, rather than prescribed.

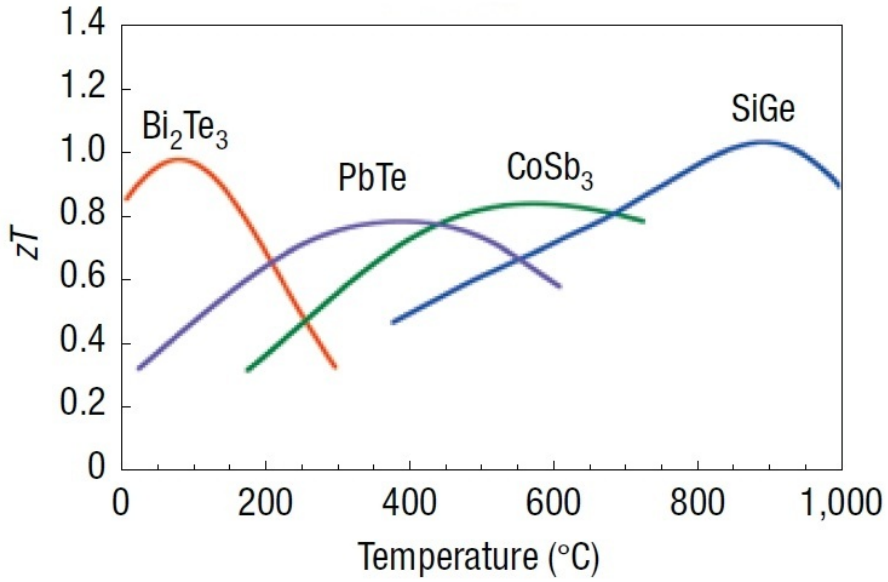

Figure 3: ZT vs. T for selected n-type thermoelectric materials [26].

For a TEG of any material, the pellet geometry can be optimized by calculating the number of thermocouples (N) and the pellet height (H) which together produce the maximum output power or efficiency for a given footprint of thermoelectric material and set of operating conditions [17]. If there are too few pellets, energy conversion will be low because the electrical resistance of a TEG will not be adequate to build up a sufficiently high voltage. Conversely, if there are too many pellets, the resistive losses will impede current flow and the power generated will be predominantly expended in heating the TEG rather than driving the load. Similarly, there is an optimal pellet height. While heat will be conducted too efficiently across short pellets, thereby reducing the temperature difference across the module, taller pellets will see increased internal resistance, which decreases the current in the module and so limits the output power.

Hodes [17] developed a procedure to optimize pellet geometry (N and H) in the case of prescribed csi and hsi temperatures and effective area, with small temperature differences allowing the Thompson effect and thermal variations in the material properties to be neglected [17]. The

procedure presented here extends that work to the more general case of prescribed ambient temperatures and hsi/csi-to-ambient thermal resistances, as depicted in Fig. 2. This extension of Hodes' model [17] more accurately models many TEG applications, such as waste heat recovery from car exhaust, where the TEG is exposed to a hot gas on one side and ambient air on the other [6]. The procedure presented here compliments that for refrigeration mode presented by Hodes [16]. However, in the case of refrigeration mode, the key geometric parameter is H, which may be optimized to maximize performance or efficiency, each creating a unique value of current supplied to a TEM. N only effects the operating voltage (and current) of a TEM operating in refrigeration mode.

II Analysis of TEGs

2.1 Prescribed, Independent, and Dependent Variables

As described by Table 1, the procedure prescribes the thermophysical properties of the pellets, temperature difference across the system, total footprint of thermoelectric material, flux-based thermal conductances from the hsi and csi to the ambient, electrical contact resistivity at the interconnects between the pellets, and load resistance in a TEG. The exception to the above is that in the sensitivity analysis in §IV, certain variables ($K''_{i-\infty,i}$, $R_{ec-\rho}$, R_L, and A_e) are considered to be independent, rather than prescribed. When efficiency is optimized (rather than performance), the output power is also prescribed. The geometry of the pellets represented by N and H are varied as independent variables, and the algorithm computes the dependent variables of efficiency, current, and in the case of performance optimization, output power.

Variable Type	Quantities	Variable(s)
Prescribed	Material properties	α, k, ρ
	Ambient temperatures at hot side, cold side	$T_{\infty,h}$, $T_{\infty,c}$
	Total footprint of thermoelectric material	A_e
	Flux-based thermal conductances from hsi, csi to ambient	$K''_{h-\infty,h}$, $K''_{c-\infty,c}$
	Load resistance	R_L
	Electrical contact resistivity at interconnects	$R_{ec-\rho}$
	Output power (In efficiency optimization case)	$\dot{W}_g$
Independent	TEG geometry: number & height of pellets	N, H
Dependent	Surface temperatures at hsi, csi	T_h, T_c
	Efficiency	η
	Current	I
	Output power (In performance optimization case)	$\dot{W}_g$

Table 1: Prescribed, independent, and dependent variables.

When bismuth telluride (Bi_2Te_3) pellets are soldered to their interconnects in conventional TEMs, the electrical contact resistivity is typically between $10^{-9}\,\Omega\cdot\mathrm{m}^2$ and $10^{-8}\,\Omega\cdot\mathrm{m}^2$ [18, 25]. Recently, Böttner *et al.* [7] and Chowdhury *et al.* [10] reported values of about $10^{-10}\,\Omega\cdot\mathrm{m}^2$ for the soldered interconnects in conventional and superlattice-type Bi_2Te_3-based TEMs, respectively, fabricated using thin-film technology, and Da Silva and Kaviany [25] concluded

that the electrical contact resistivity of Bi_2Te_3-metal interfaces may be reduced to or below $2 \times 10^{-11}\,\Omega \cdot m^2$. The electrical contact resistivity at heavily doped Si-metal interfaces may, in theory, be as low as about $10^{-13}\,\Omega \cdot m^2$ [9, 18].

The flux-based conduction through the ceramic substrate of a typical TEM is about $28000\,W/m^2K$, increasing to $210000\,W/m^2K$ if beryllia is used instead of the usual alumina [8, 21, 28, 29]. Additionally, Chowdhury *et al.* [10] showed that the the conduction through a typical solder interface will only reach $125000\,W/m^2K$ or so, though can be as high as $1000000\,W/m^2K$ for superlattice-metal interfaces. This indicates that even if a theoretical heat sink has zero thermal resistance, there is still an upper limit on $K''_{i-\infty,i}$.

2.2 Assumptions, Limitations and Conventions

The work presented here is for a one-dimensional model neglecting lateral flow of heat and charge. Given the moderate temperature ranges analyzed ($\lesssim 100^\circ C$), the Thompson effect is assumed to be negligible, the material properties can be approximated as constants, and use of a single thermoelectric material is appropriate. We assume that ρ, k, and $|\alpha|$ are the same for both n- and p-type pellets.

It is of note that this analysis calculates the optimal number of thermocouples in an array. If the total area of the pellets exceeds a few centimeters per side, it would be necessary to divide the array into M modules, each less than 5 cm on a given side, to reduce the effects of thermal expansion. The calculations for a module or an array are equivalent, provided the number of thermocouples is the same for both.

For the purposes of simplicity, the examples in this paper use $K''_{h-\infty,h} = K''_{c-\infty,c}$, collectively defined as $K''_{i-\infty,i}$, but the algorithm can operate equally well if they are taken to be distinct values.

The pellet packing density is arbitrary, but its value will impact the footprint of the heat sinks attached to a TEM, and the $K''_{i-\infty,i}$ values will be somewhat dependent on it.

The movement of heat across a semiconductor causes its charge carriers (electrons in n-type materials and holes in p-type materials) to flow in that direction, as seen in Fig. 2. Therefore, when the pellets are connected as shown, positive charge carriers flow from n- to p-type pellets at the cold side (i.e. counterclockwise according to Fig. 2) [17, 18]. By convention, this is defined as the positive current direction. The sign convention for the voltage difference across a TEM ($V_{TEM} = V_o - V_N$) is such that a positive voltage produces a positive current; therefore, V_{TEM} in Fig. 1 is positive [18].

2.3 Governing Equations

In order to develop the governing equations, we must first define some thermal and electrical quantities. The Ohmic resistance, electrical contact resistance and thermal conductance of a thermocouple are conventionally defined [17], respectively, as

$$R = \frac{2\rho H}{A_p} \tag{1}$$

$$R_{ec-R} = \frac{4R_{ec-\rho}}{A_p} \tag{2}$$

$$K = \frac{2kA_p}{H}. \tag{3}$$

Expressing pellet cross-sectional area in terms of the effective footprint of a TEG (A_e), it equals

$$A_p = \frac{A_e}{2N}. \tag{4}$$

It follows that in terms of A_e, the quantities R, R_{ec-R} and K are

$$R = \frac{4N\rho H}{A_e} \tag{5}$$

$$R_{ec-R} = \frac{8NR_{ec-\rho}}{A_e} \tag{6}$$

$$K = \frac{kA_e}{NH}. \tag{7}$$

We apply surface energy balances at the hsi and csi and they yield, respectively,

$$\begin{aligned}
\left(T_{\infty,h}-T_h\right)/R_{h-\infty,h} &= N\left[I\alpha_{p,n}T_h - K\left(T_h-T_c\right) - I^2(R+R_{ec-R})/2\right] &(8)\\
\left(T_c-T_{\infty,c}\right)/R_{c-\infty,c} &= N\left[I\alpha_{p,n}T_c - K\left(T_h-T_c\right) + I^2\left(R+R_{ec-R}\right)/2\right]. &(9)
\end{aligned}$$

The difference between (8) and (9) equals the output power of the TEG,

$$\dot{W}_g = NI\left[\alpha_{p,n}\left(T_h-T_c\right) - I\left(R+R_{ec-R}\right)\right], \tag{10}$$

where the term $NI\alpha_{p,n}\left(T_h-T_c\right)$ accounts for the Peltier effect, and the term $NI^2\left(R+R_{ec-R}\right)$ is energy lost through ohmic heating in the bulk material and in the electrical contacts. The voltage generated across the TEM is the output power divided by the current, i.e.,

$$V_{TEM} = N\left[\alpha_{p,n}\left(T_c-T_h\right) + I\left(R+R_{ec-R}\right)\right]. \tag{11}$$

2.4 Solving the Equations

2.4.1 Performance Optimization

The surface energy balances in (8) and (9) are first solved simultaneously for T_h and T_c. Once these are known, we can apply (5) - (7) and note that Ohm's Law implies that $\dot{W}_g(I,N,H) = I^2R_L$. Then (10) becomes

$$\begin{aligned}
I^2R_L = {} & \{-A_{sub}NI\{A_{sub}H\times\left[A_e\alpha_{p,n}\left(T_{\infty,c}-T_{\infty,h}\right)+4NI\left(2R_{ec-\rho}+H\rho\right)\right]\\
& +NI[-2NHI\alpha_{p,n}\left(R''_{c-\infty,c}-R''_{h-\infty,h}\right)\left(2R_{ec-\rho}+H\rho\right)+A_e\left[H\alpha^2_{p,n}\left(R''_{h-\infty,h}T_{\infty,c}+R''_{c-\infty,c}T_{\infty,h}\right)\right]\\
& +4k\left(R''_{c-\infty,c}+R''_{h-\infty,h}\right)\left(2R_{ec-\rho}+H\rho\right)]\}\}\\
& /\{A_e[A^2_{sub}H+A_eA_{sub}k\left(R''_{c-\infty,c}+R''_{h-\infty,h}\right)+A_{sub}NHI\alpha_{p,n}\left(R''_{c-\infty,c}-R''_{h-\infty,h}\right)\\
& -N^2HI^2\alpha^2_{p,n}R''_{c-\infty,c}R''_{h-\infty,h}]\},
\end{aligned} \tag{12}$$

from which the current can be calculated for a given N, H pair. Unlike the analysis using constant T_h and T_c boundary conditions [17], however, the current cannot be solved for analytically.

To optimize the geometry, this equation is solved numerically to find the current as a function of pellet height and number of thermocouples. We can maximize the function $I(N,H)$ in two dimensions and determine the values of N and H that yield the largest current, or equivalently, output power. The optimal output power can be calculated by evaluating $I_{max}^2 R_L$.

Thus, the algorithm computes the optimal N, H pair which maximizes output power. Currently, N and H are not optimized in practice; therefore, this is of substantial value. For a more precise optimization, the values calculated from the algorithm may be used as an initial guess for a numerical optimization that accounts for, e.g., the variable thermophysical properties of the pellets.

2.4.2 Efficiency Optimization

To optimize efficiency, we further prescribe the desired output power of the TEG. T_c and T_h are first calculated as in the performance optimization algorithm. The efficiency is equal to the output power divided by the rate of heat input, and it follows from (8) that

$$\eta = \frac{\dot{W}_g}{N\left[I\alpha_{p,n}T_h - K\left(T_h - T_c\right) - I^2(R+R_{ec-R})/2\right]}. \tag{13}$$

The function $\eta(N,H)$ is then maximized numerically. Because the performance is prescribed in this algorithm, this optimization must be constrained to values of N and H which generate the prescribed value of $\dot{W}_g$. It is generally not the case that the geometry yielding the maximum performance will correlate to the maximum efficiency. At the maximum output power, there is a unique efficiency. As the prescribed value of $\dot{W}_g$ is relaxed to lower values, the range of possible values of η expands, allowing for higher efficiencies.

It is possible that for a particular set of operating conditions, there will be no geometries which are capable of producing the prescribed output power. In this case, the operating condi-

tions should be reassessed using the performance optimization algorithm to achieve the requisite output power.

III RESULTS

3.1 Illustrative Example

Our baseline operating conditions are shown in Table 2. We take $T_{\infty,i}$, A_e, R_L and $R_{ec-\rho}$ from the values used in Hodes' example [17]. We assume a pellet packing density of $\phi = 40\,\%$, which gives a module footprint ($A_{sub} = A_e/\phi$) of $1562\,\mathrm{mm}^2$. The thermal conductances between the hsi and csi and the ambient are set equal to $K = 4\,\mathrm{W/K}$, typical of the values for an air-cooled heat sink of footprint A_{sub} [1]. It follows that $K''_{i-\infty,i} = 2500\,\mathrm{W}/\left(\mathrm{m}^2\mathrm{K}\right)$. For the efficiency analysis, we increase this value to $K''_{i-\infty,i} = 4000\,\mathrm{W}/\left(\mathrm{m}^2\mathrm{K}\right)$ in order to provide the prescribed output power of 1 W. Since the module will be operating between approximately 20°C and 100° C, we use bismuth telluride as the thermoelectric material. We take the thermoelectric properties of Bi_2Te_3 at the mean temperature of 60°C from [2], given in Table 2

Variable	Value
$T_{\infty,c}$	$20^\circ\,\mathrm{C}$
$T_{\infty,h}$	$100^\circ\,\mathrm{C}$
$K''_{h-\infty,h}$	Performance: $2500\,\mathrm{W}/\left(\mathrm{m}^2\cdot\mathrm{K}\right)$
	Efficiency: $4000\,\mathrm{W}/\left(\mathrm{m}^2\cdot\mathrm{K}\right)$
$K''_{c-\infty,c}$	Performance: $2500\,\mathrm{W}/\left(\mathrm{m}^2\cdot\mathrm{K}\right)$
	Efficiency: $4000\,\mathrm{W}/\left(\mathrm{m}^2\cdot\mathrm{K}\right)$
R_L	$5\,\Omega$
$R_{ec-\rho}$	$10^{-9}\,\Omega\cdot\mathrm{m}^2$
ϕ	$40\,\%$
A_e	$625\,\mathrm{mm}^2$
$\alpha_{p,n}$	$416\,\mu\mathrm{V/K}$
k	$1.54\,\mathrm{W}/\left(\mathrm{m}\cdot\mathrm{K}\right)$
ρ	$11.9\,\mu\Omega\cdot\mathrm{m}$
$\dot{W}_g$	Efficiency: 1 W

Table 2: Baseline operating conditions. Unmarked values are used in both performance and efficiency optimizations.

Using these values, we find that output current varies over H and N as shown in Fig. 4 and note the presence of a global maximum, where $N = 229$ ($A_p = 1.04\,\mathrm{mm}^2$), $H = 0.83\,\mathrm{mm}$, and $\dot{W}_g = 1.5\,\mathrm{W}$.

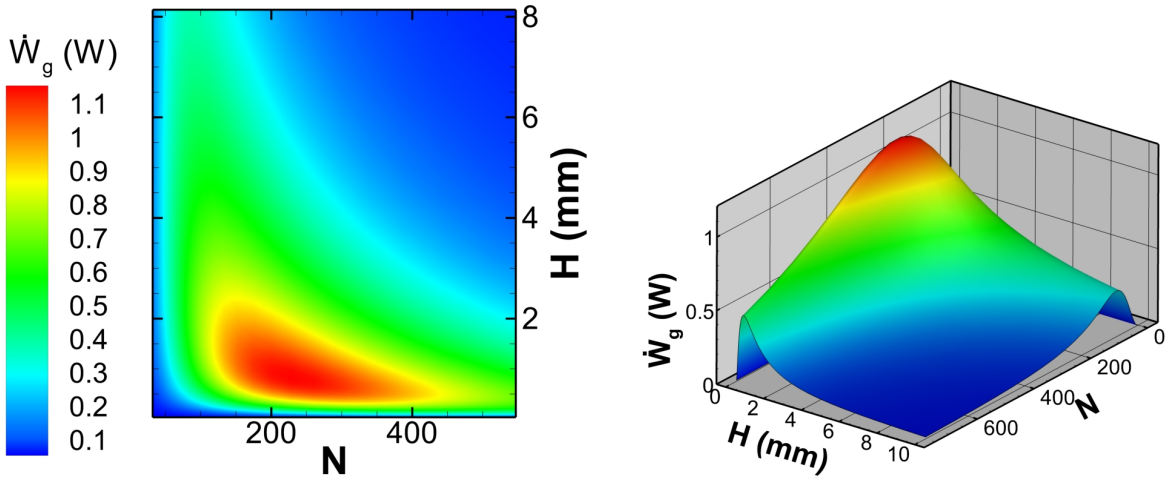

Figure 4: Contour (left) and surface (right) plots of $\dot{W}_g(N,H)$ for baseline operating conditions ($T_c = 20°\mathrm{C}$, $T_h = 100°\mathrm{C}$, $A_e = 625\,\mathrm{mm}^2$, $R_L = 5\,\Omega$, $R_{ec-\rho} = 10^{-9}\,\Omega\cdot\mathrm{m}^2$, $K''_{i-\infty,i} = 2500\,\mathrm{W/m}^2\cdot\mathrm{K}$).

Using the same baseline conditions with a prescribed power output of 1 W and $K''_{i-\infty,i} = 4000\,\mathrm{W/(m^2K)}$ in order to allow that value, we apply the efficiency optimization algorithm. Fig. 5 shows an overlay of the output power and efficiency of a TEG as N and H vary. In order to perform the optimization, we must constrain N and H to values which provide the requisite output power, i.e. along the contour line labeled "1 W" . The algorithm finds the optimal efficiency to be 2.8 % at $N = 138$ and $H = 2.4\,\mathrm{mm}$. It is worth noting that the efficiency is constrained by the Carnot efficiency (η_c) and the limit for the thermoelectric material (η_{max}) [17],

$$\eta_c = 1 - T_{\infty,c}/T_{\infty,h} = 21.4\,\% \tag{14}$$

$$\eta_{max} = \frac{\gamma - 1}{\gamma + T_{\infty,c}/T_{\infty,h}}\eta_c = 3.4\,\%, \tag{15}$$

where $\gamma = \sqrt{1+ZT_M}$.

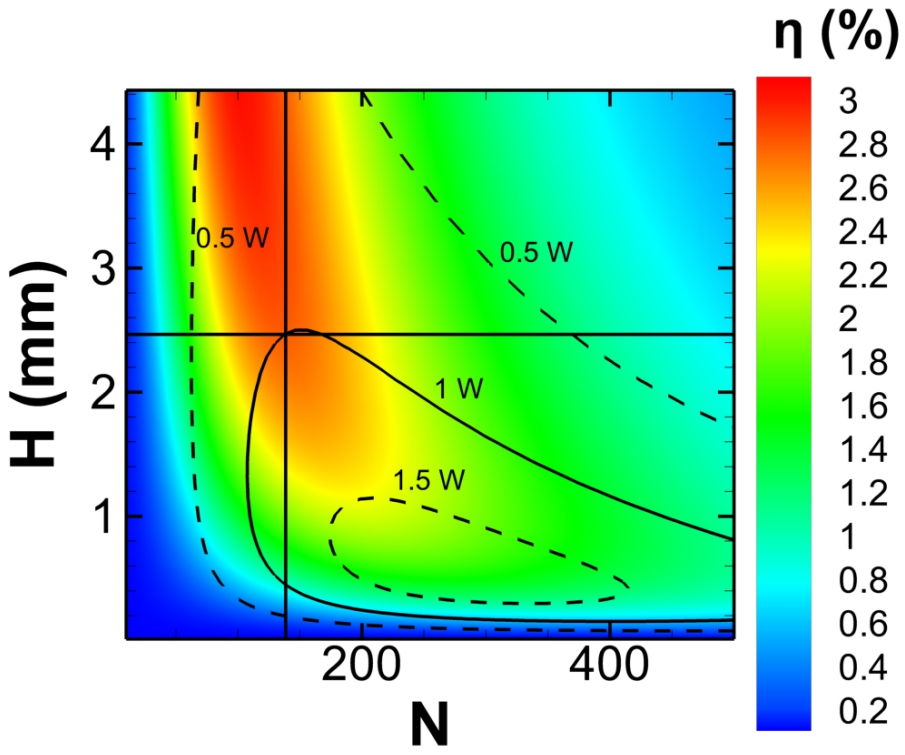

Figure 5: Overlaid contour plots of η (color map) and $\dot{W}_g$ (contour lines), over a range of N and H for baseline conditions with $K''_{i-\infty,i} = 4000\,\mathrm{W}/\left(\mathrm{m}^2\cdot\mathrm{K}\right)$. The crosshairs indicate the calculated optimal efficiency of 2.8 % at $N = 138$ and $H = 2.4\,\mathrm{mm}$, yielding a power of 1.0 W.

3.2 Validation

In order to validate the model, we show that as $K''_{i-\infty,i} \to \infty$, the model yields results consistent with those in the literature. Hodes' model in [17] can be viewed as a subset of the current work in which $K''_{i-\infty,i}$ are assumed to be infinite, such that the hsi and csi temperatures T_i are equal to the corresponding ambient temperature, $T_{\infty,i}$. Because the value of H which maximizes performance approaches zero as $K''_{i-\infty,i} \to \infty$, we take a constant value of $H = 3.5\,\mathrm{mm}$ for this assessment. Fig. 6 shows that as $K''_{i-\infty,i}$ increases, $\dot{W}_g(N)$ and $\eta(N)$ converge to the results calculated by Hodes in [17,18]. Additionally, the degradation of the performance and efficiency attributable to irreversibility due to the hsi-to-ambient and csi-to-ambient thermal resistances is apparent.

We see in Fig. 6 that as $K''_{i-\infty,i} \to \infty$, the maximum power and optimized N, H saturate to the values calculated using the equations in [17] for performance optimization for fixed A_e

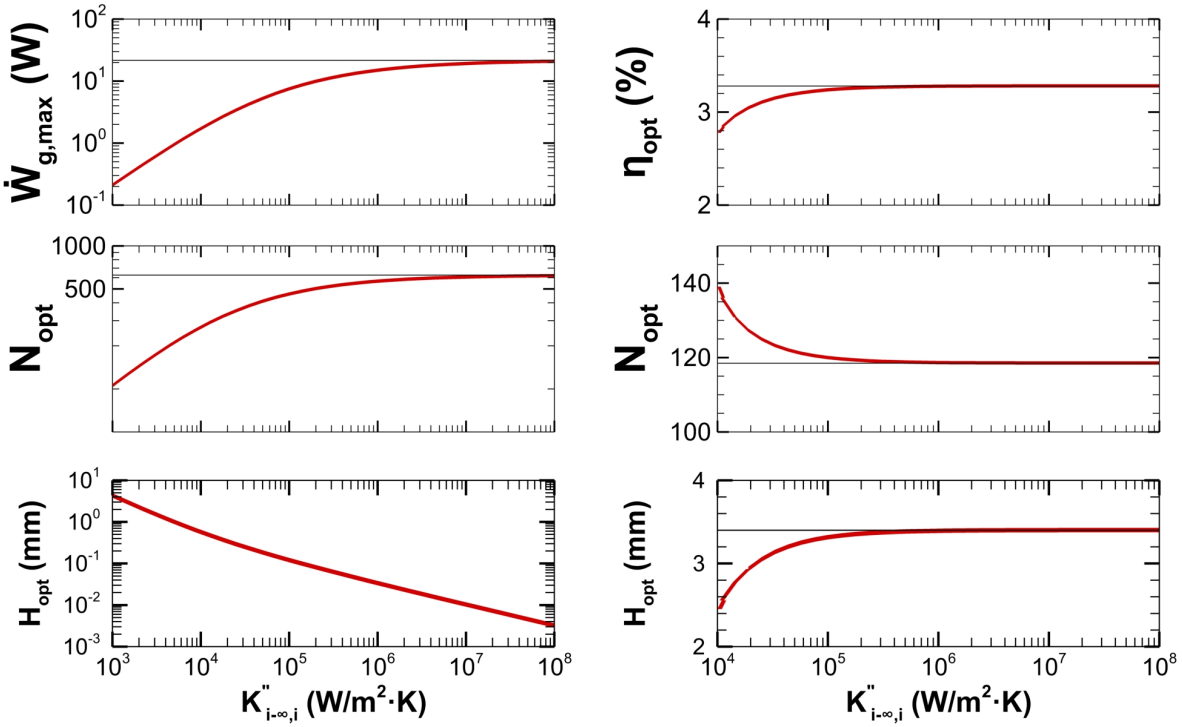

Figure 6: Convergence of performance (left) and efficiency (right) to Hodes' model [17] as $K''_{i-\infty,i} \to \infty$, for baseline conditions. Shown on the plot are the constant lines at the optimized values from Hodes' model (For performance, top: $\dot{W}_{g,max} \to 21.619\,\mathrm{W}$; middle: $N_{opt} \to 625$; bottom: $H_{opt} \to 0\,\mathrm{mm}$. For efficiency, top: $\eta_{opt} \to 3.28\,\%$; middle: $N_{opt} \to 118.5$; bottom: $H_{opt} \to 3.41\,\mathrm{mm}$).

and finite $R_{ec-\rho}$ (i.e., $\dot{W}_{g,max} \to 21.619\,\mathrm{W}$, $N_{opt} \to 625$ and $H_{opt} \to 0\,\mathrm{mm}$) under the baseline conditions.

The same convergence is seen with efficiency in Fig. 6, with the maximum constrained efficiency and optimized N and H yielding it saturating to $\eta_{max} \to 3.28\,\%$, $N_{opt} \to 118$, and $H_{opt} \to 3.4\,\mathrm{mm}$ for baseline conditions with $\dot{W}_g = 1\,\mathrm{W}$. The allowable geometries are reduced (and therefore the achievable efficiency decreased) as the performance is more highly constrained. For example, for an analysis constrained to the maximum possible power ($\dot{W}_g = 3.4\,\mathrm{W}$, occurring at $N = 229$ and $H = 0.83\,\mathrm{mm}$), there is a unique allowable solution which provides an efficiency of only $0.48\,\%$.

IV SENSITIVITY ANALYSIS

The optimal pellet geometry is rather sensitive to the operating conditions. In the previous example, we see in Fig. 4 that near the maximum output power, the optimization is more sensitive to decreases in N and H than increases in them. This indicates that in an imprecise model, it may be advisable to err on the higher side of the theoretical optimal values.

4.1 hsi-to-Hot-Side & csi-to-Cold-Side Thermal Conductance

We see in Fig. 7 and Fig. 8 that as the thermal conductance from the hsi and csi to the ambients increases, the current output saturates to a constant value (consistent with the results from [17], as seen in Fig. 6), indicating that the system has reduced to the constant-temperature boundary condition problem ($T_i \to T_{\infty,i}$). This saturation point is somewhat dependent upon the other operating conditions. Similarly, as conductance approaches zero, the current decreases as a TEM becomes more insulated from the ambient. The output power curve exhibits the same behavior as the current. These results indicate that past a certain point, a heat sink can be considered sufficiently large, and further enhancements will result in minimal performance increase.

Increasing $K''_{i-\infty,i}$ also causes N_{opt} to increase up to a saturation point, while H_{opt} decreases continuously.

4.2 Electrical Contact Resistivity

Increasing the electrical contact resistivity at the interconnects causes a decrease in the current or power that a TEG produces. However, we can see in Fig. 8 and Fig. 10 that at a certain point, the performance saturates and the increase in performance for further decreasing electrical contact resistivity becomes negligible. This indicates that when choosing materials for a given application, there is no need to reduce $R_{ec-\rho}$ below a certain saturation point. In the example shown in Fig. 10, the saturation point is around $R_{ec-\rho} = 10^{-9}\,\Omega \cdot \mathrm{m}^2$, but this is heavily dependent on the other operating parameters. For example, as $K''_{i-\infty,i}$ increases, the saturation point of $R_{ec-\rho}$ decreases so that for very high $K''_{i-\infty,i}$, having a very low electrical contact re-

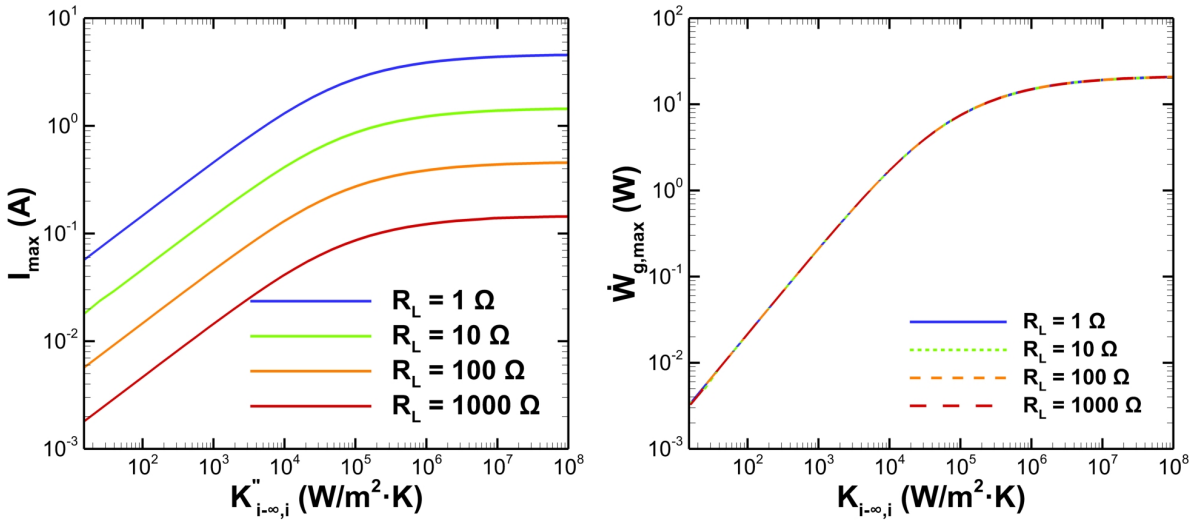

Figure 7: Sensitivity of maximum current (left) and output power (right) to changes in $K''_{i-\infty,i}$ and load under baseline operating conditions.

sistivity becomes much more important to obtain the maximum performance, as seen in Fig. 9. However, a typical heat sink will not provide $K''_{i-\infty,i} \gtrsim 10^4\,\mathrm{W/m^2K}$, implying that past a certain point, decreasing $R_{ec-\rho}$ indefinitely will not yield further improvements.

The effect of $R_{ec-\rho}$ on N_{opt} and H_{opt} is also observed. As $R_{ec-\rho}$ increases from zero, the optimal number of pellets decreases, while the optimal pellet height increases.

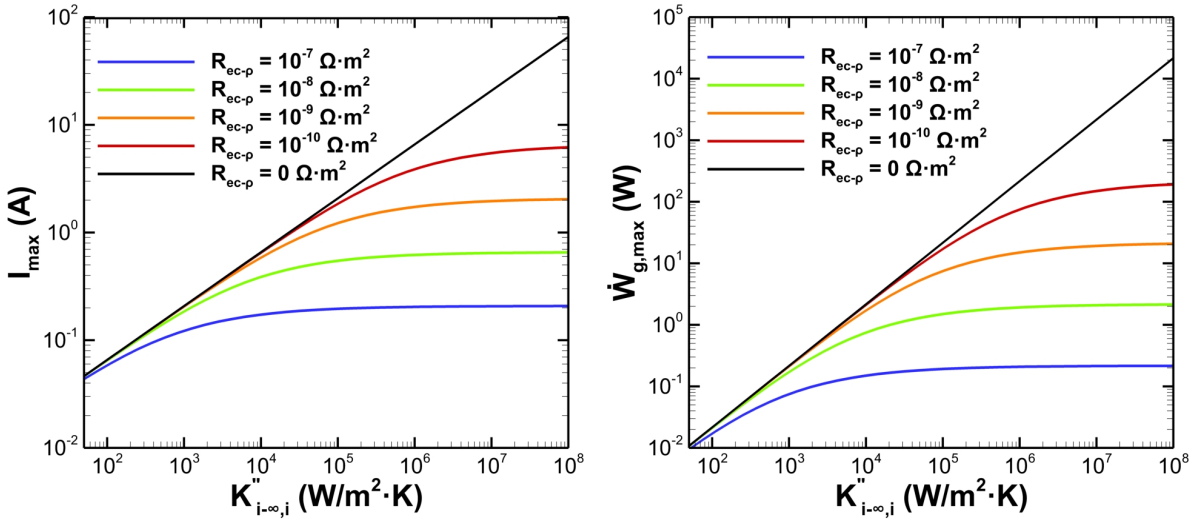

Figure 8: Sensitivity of maximum current (left) and output power (right) to changes in thermal conductance and electrical contact resistivity with baseline operating conditions.

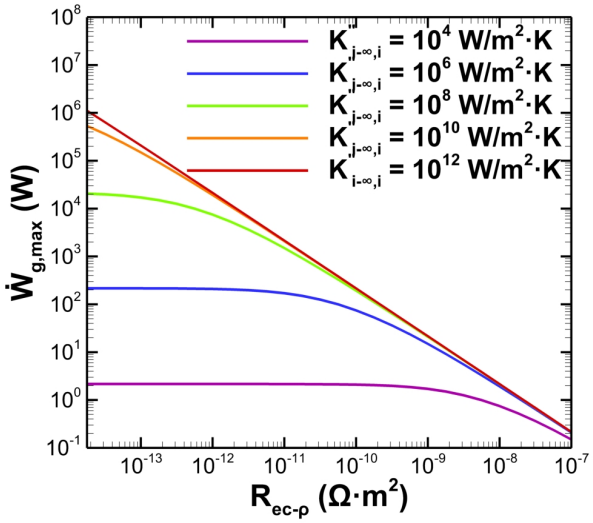

Figure 9: Sensitivity of saturation point of $R_{ec-\rho}$ to changes in $K''_{i-\infty,i}$.

4.3 Load

In Fig. 7 and Fig. 10, we can see that a TEG will produce more current when the load resistance is smaller. However, the output power is not affected by changes in R_L, since current decreases while resistance increases such that $\dot{W}_g = I^2 R_L$ remains constant. We also find that increasing R_L increases the optimal number of pellets, but does not affect the optimal pellet height.

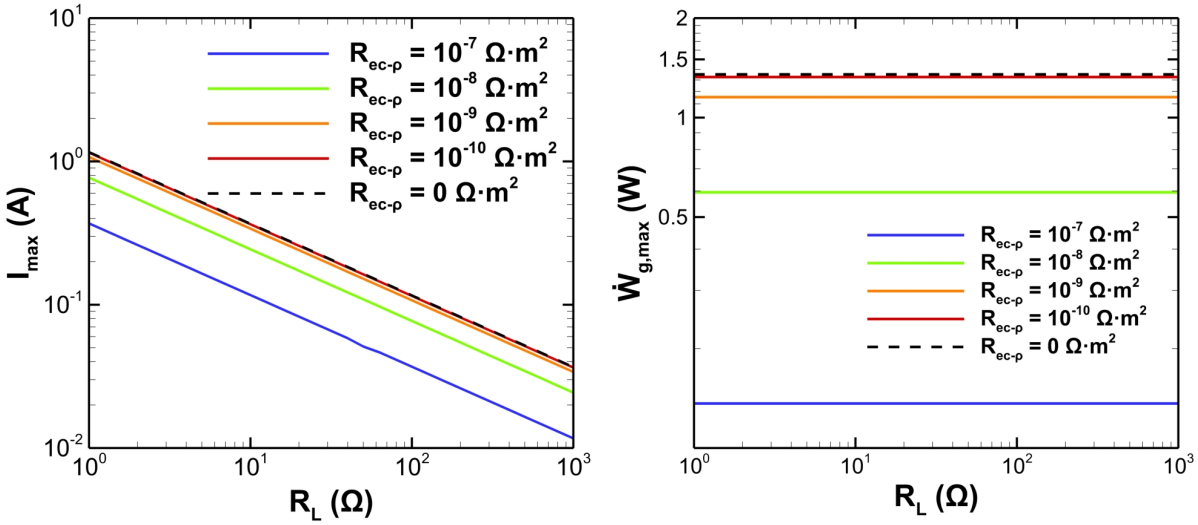

Figure 10: Sensitivity of maximum current (left) and output power (right) to changes in load and electrical contact resistivity with baseline operating conditions.

4.4 Effective Area

The prescribed A_e has a significant effect on the maximum output power or efficiency that can be attained, as seen in Fig. 11. Increasing A_e will always increase the output power. However, for the efficiency optimization case, the efficiency cannot exceed η_{max} for the thermoelectric material, i.e., 3.4 % for Bi_2Te_3. Therefore, efficiency saturates as A_e increases. We also see limits on the allowed geometries in the efficiency optimization case. If the module's footprint is too small, the prescribed output power is not possible. On the other hand, at a certain point the geometry of a theoretically optimal TEG becomes unrealistic (i.e., pellet heights of 10 mm). Fig. 11 also shows that as the prescribed $\dot{W}_g$ increases, the range of allowable geometries and the maximum possible efficiency are reduced.

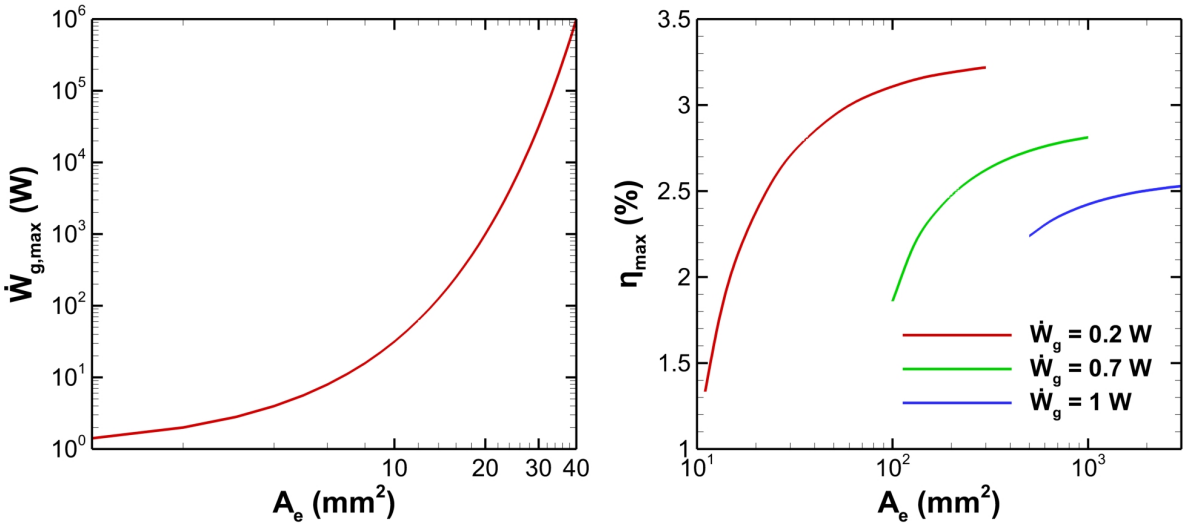

Figure 11: Sensitivity of performance (left) and efficiency (right) to A_e. For the efficiency plot, $\dot{W}_g$ is prescribed at three different values (0.2 W, 0.7 W and 1 W)

4.5 Temperature

As expected, the output power is highly dependent on the ambient temperatures. Fig. 12 shows that as $\Delta T = T_{\infty,h} - T_{\infty,c}$ decreases, the output power drops to zero as there is no temperature difference to drive the thermoelectric effects. For a given ΔT regardless of the individual temperatures, the power output will be constant. However, this is only the case under the as-

sumption of constant material properties. In reality, changes in the temperatures would affect the material properties, possibly to the point that a different material is recommended. In addition, as the absolute temperatures increase, the Thompson effect and the merits of segmentation will require consideration.

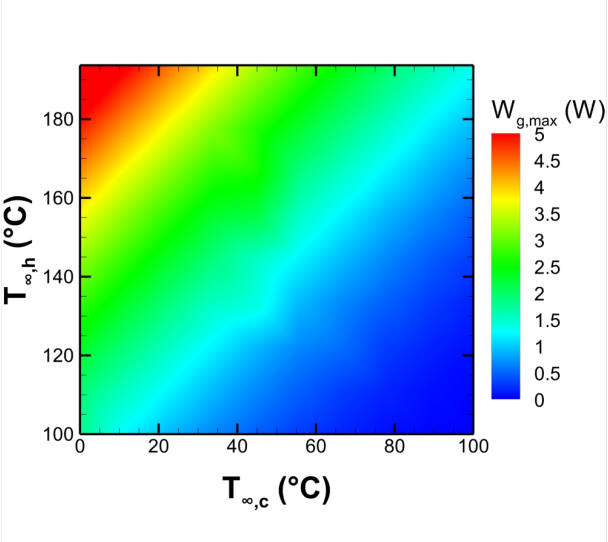

Figure 12: Sensitivity of maximum output power to $T_{\infty,c}$ and $T_{\infty,h}$.

V CONCLUSIONS

The algorithm described optimizes TEG geometry (N and H) and provides a significant increase in power output over generic TEGs. Embedding a TEG in a thermal resistance network as per this analysis is more broadly useful than previously seen analyses where the hsi and csi temperatures have been prescribed. The analysis also allows one to determine which adjustments to operating and packaging parameters will result in the most improvement in performance or efficiency. Future work generalizing the analysis to account for temperature-dependent thermoelectric properties and allowing for segmentation of the thermoelectric pellets would allow for application of the algorithm to situations with larger temperature differences. Further generalizations could also allow for variable bulk temperatures.

REFERENCES

[1] Aavid - thermal engineering and heat sink manufacturing - online store. http://www.aavid.com/.

[2] Melcor thermal solutions, 2002.

[3] Stanley W. Angrist. *Direct Energy Conversion*. Allyn and Bacon Series in Mechanical Engineering and Applied Mechanics. Allyn and Bacon, Inc., fourth edition, 1982.

[4] Incorporated BCS. Waste heat recovery: Technology and opportunities in U.S. industry. Technical report, March 2008.

[5] L. E. Bell. Cooling, heating, generating power, and recovering waste heat with thermoelectric systems. *Science*, 321(5895):1457–1461, September 2008.

[6] T. Bergman, A. Lavine, F. Incro, and D. DeWitt. *Fundamentals of Heat and Mass Transfer*. Wiley, 7 edition, April 2011.

[7] H. Bottner, J. Nurnus, A. Gavrikov, G. Kuhner, M. Jagle, C Jybzek, D. Eberhard, G. Plescher, A. Schubert, and K.-H. Schlereth. New thermoelectric components using microsystem technologies. *J. Microelectromech. Syst.*, 13(3):414–420, June 2004.

[8] {Ceram Research}. Beryllium oxide - beryllia. http://www.azom.com/article.aspx?ArticleID=263, April 2001.

[9] C. Y. Chang, Y. K. Fang, and S. M. Sze. Specific contact resistance of metal-semiconductor barriers. *Solid-State Electron.*, 14(7):541, 1971.

[10] I. Chowdhuy, R. Prasher, K. Lofgreen, G. Chrysler, S. Narasimhan, R. Mahajan, D. Koester, R. Alley, and R. Venkatasubramaniani. On-chip cooling by superlattice-based thin-film thermoelectrics. *Nature Nanotechnol.*, 4:235–238, January 2009.

[11] Z.H. Dughaish. Lead telluride as a thermoelectric material for thermoelectric power generation. *Physica B: Condensed Matter*, 322(1–2):205–223, September 2002.

[12] Mohamed S. El-Genk and Hamed H. Saber. High efficiency segmented thermoelectric unicouple for operation between 973 and 300 k. *Energy Conversion and Management*, 44(7):1069–1088, May 2003.

[13] Dr. Terry Hendricks and William T. Choate. Engineering scoping study of thermoelectric generator systems for industrial waste heat recovery. Technical report, DOE Industrial Technologies Program, November 2006.

[14] Corey A. Hewitt, Alan B. Kaiser, Siegmar Roth, Matt Craps, Richard Czerw, and David L. Carroll. Multilayered carbon Nanotube/Polymer composite based thermoelectric fabrics. *Nano Letters*, 12(3):1307–1310, 2012.

[15] M. Hodes. On one-dimensional analysis of thermoelectric modules (TEMs). *Components and Packaging Technologies, IEEE Transactions on*, 28(2):218 – 229, June 2005.

[16] M. Hodes. Optimal pellet geometries for thermoelectric refrigeration. *Components and Packaging Technologies, IEEE Transactions on*, 30(1):50–58, 2007.

[17] M. Hodes. Optimal pellet geometries for thermoelectric power generation. *Components and Packaging Technologies, IEEE Transactions on*, 33(2):307–318, 2010.

[18] Marc Hodes. Optimal design of thermoelectric refrigerators embedded in a thermal resistance network. *Components, Packaging and Manufacturing Technology, IEEE Transactions on*, 2(3):483–495, March 2012.

[19] M. Koshigoe, Y. Kudo, M. Hashimoto, I. Shiota, and I.A. Nishida. Thermoelectric properties of segmented Bi2Te3/PbTe. In *Thermoelectrics, 1998. Proceedings ICT 98. XVII International Conference on*, pages 479–482, 1998.

[20] A. Kosuga, K. Kurosaki, H. Muta, and S. Yamanaka. Thermoelectric properties of n-type ag-pb-sb-te compounds. In *Thermoelectrics, 2005. ICT 2005. 24th International Conference on*, pages 45– 48, 2005.

[21] Myer Kutz. Precision temperature control using a thermoelectric module. In *Heat Transfer Calculations*. McGraw-Hill Professional.

[22] Laifeng Li, Zhen Chen, Min Zhou, and Rongjin Huang. Developments in semiconductor thermoelectric materials. *Frontiers in Energy*, 5(2):125–136, April 2011.

[23] Shashank Priya, D. J Inman, and Snyder. Chapter 11: Thermoelectric energy harvesting. In *Energy harvesting technologies*. Springer, New York; London, 2008.

[24] E. J Sandoz-Rosado. *Investigation and development of advanced models of thermoelectric generators for power generation applications*. PhD thesis, Rochester Institute of Technology, 2009.

[25] L. W. Silva and M. Kaviany. Micro-thermoelectric cooler: Interfacial effects on thermal and electrical transport. *Int. J. Heat Mass Trans.*, 47(10-11):2417–2435, May 2004.

[26] G. Jeffrey Snyder and Eric S. Toberer. Complex thermoelectric materials. *Nature Materials*, 7(2):105–114, February 2008.

[27] J. Yang. Potential applications of thermoelectric waste heat recovery in the automotive industry. In *Thermoelectrics, 2005. ICT 2005. 24th International Conference on*, pages 170–174, 2005.

[28] M. M. Yovanovich, J.R. Culham, and P. Teertstra. Modeling thermal resistance of diamond spreader on copper heat sink systems. Austin, TX, September 1996.

[29] M. M. Yovanovich, C.H. Tien, and G.E. Schneider. General solution of constriction resistance within a compound disk. *Heat Transfer, Thermal Control and Heat Pipes, AIAA Progress in Astronautics and Aeronautics*, 70, 1980.

[30] Jen-Kan Yu, Slobodan Mitrovic, Douglas Tham, Joseph Varghese, and James R. Heath. Reduction of thermal conductivity in phononic nanomesh structures. *Nat Nano*, 5(10):718–721, October 2010.

[31] Rui Zhang, Marc Hodes, David A. Brooks, and Vincent P. Manno. Optimized thermoelectric module-heat sink assemblies for precision temperature control. *Journal of Electronic Packaging*, 134(2), June 2012.